Mechanically stimulated osteocytes maintain tumor dormancy in bone metastasis of non-small cell lung cancer by releasing small extracellular vesicles

Jing Xie[1,2,5], Yafei Xu[1,5], Xuhua Liu[4], Li Long[2], Ji Chen[2], Chunyan Huang[2], Yan Shao[4], Zhiqing Cai[2], Zhimin Zhang[2], Ruixin Zhou[2], Jiarong Leng[3], Xiaochun Bai[2, 4] ✉ and Qiancheng Song[2, 3] ✉

[1]General Practice Centre, The Seventh Affiliated Hospital, Southern Medical University, Foshan, Guangdong, 528000, China.

[2]Guangdong Provincial Key Laboratory of Bone and Joint Degeneration Diseases, Department of Cell Biology, School of Basic Medical Sciences, Southern Medical University, Guangzhou, 510515, China.

[3]Department of Neurosurgery, Institute of Brain Diseases, Nanfang Hospital of Southern Medical University, Guangzhou, 510515, China.

[4]Academy of Orthopedics, Guangdong Province, Guangdong Provincial Key Laboratory of Bone and Joint Degeneration Diseases, The Third Affiliated Hospital of Southern Medical University, Guangzhou, 510630, China.

[5]These authors contributed equally: Jing Xie, Yafei Xu.

✉ email: baixc15@smu.edu.cn; songqc@smu.edu.cn

Abstract

Although preclinical and clinical studies have shown that exercise can inhibit bone metastasis progression, the mechanism remains poorly understood. Here, we found that non-small cell lung cancer (NSCLC) cells adjacent to bone tissue had a much lower proliferative capacity than the surrounding tumor cells. Subsequently, it was demonstrated that osteocytes, sensing mechanical stimulation generated by exercise, inhibit NSCLC cell proliferation and sustain the dormancy thereof by releasing small extracellular vesicles with tumor suppressor microRNAs, such as miR-99b-3p. Furthermore, mechanical loading of the tibia inhibited the bone metastasis progression of NSCLC. Notably, bone metastasis progression of NSCLC was inhibited by moderate exercise, and combinations with zoledronic acid had additive effects. Moreover, exercise preconditioning effectively suppressed bone metastasis progression. This study significantly advances the understanding of the mechanism underlying exercise-afforded protection against bone metastasis progression.

30 ## Introduction

31 Lung cancer is the second most common cancer type and the leading global cause of cancer
32 mortality (18.0% of the total cancer deaths) [1]. Approximately 85% of lung cancer patients have a
33 group of histological subtypes collectively termed non-small cell lung cancer (NSCLC) [2]. Despite
34 important advancements in NSCLC treatment that have been achieved over the past two decades,
35 prognosis remains poor owing to the presence of locally advanced or widely metastatic tumors in
36 most patients at the time of diagnosis [2]. Approximately 20% – 30% of patients with NSCLC
37 present with bone metastases at diagnosis, and 35% – 60% will develop them during their disease
38 course [3,4]. Bone metastases are frequent events associated with advanced-stage malignancies and
39 often cause skeletal-related events (SREs) such as severe bone pain, pathological fractures, spinal
40 cord compression, and hypercalcemia, which reduce the quality of life and predict a poor
41 prognosis [3,5,6]. In general, bone metastases are incurable; goals of management include
42 maximizing symptom control, preserving function, minimizing SREs, and enhancing local tumor
43 control [2,7]. A multi-disciplinary treatment approach is required, including pain management,
44 osteoclast inhibitors and other bone-specific therapy, systemic anti-cancer therapy, surgery,
45 radiation, and interventional techniques. Although there have been many advances in treatment,
46 the median survival from diagnosis of bone metastases has been reported to be very short in
47 patients with lung cancer [2,7]. Therefore, it is of considerable clinical significance to elucidate the
48 mechanism of bone metastasis and to find new drugs and combination therapies for bone
49 metastasis prevention and treatment in NSCLC.

50 Many preclinical and clinical studies have shown that exercise can reduce the incidence of
51 various cancers, inhibit cancer progression, reduce symptom burden, mitigate side effects of

52 cancer treatment, and improve survival and the quality of life in patients with cancer [8-11]. In
53 contrast, sedentary behavior and lack of physical activity is positively associated with an increased
54 risk for cancer and mortality [12,13]. Exercise is safe perioperatively, and multiple international
55 organizations have published exercise recommendations for patients with cancer [10,11,14]. The
56 evidence to-date suggests a benefit of exercise in all stages of lung cancer and lung cancer
57 survivors [10]. Exercise has the potential to improve physical function and the quality of life in
58 individuals with bone metastases and appears safe and feasible when it includes an element of
59 supervised exercise instruction [11,15]. The optimal exercise prescription for patients with bone
60 metastases is currently undefined [14,16]. Each patient with cancer may require a more personalized
61 exercise prescription. Therefore, a clearer understanding of the mechanisms by which exercise
62 modulates tumors is required.

63 Exercise induces systemic changes involving every system over the entire body, including
64 circulating substances, the immune system, and metabolism [17-19]. Throughout life, the skeleton
65 undergoes continuous remodeling, which is a balance between the resorption of mineralized bone
66 by bone-resorbing cells (osteoclasts) and new bone formation by bone-forming cells (osteoblasts)
67 [20]. Osteocytes, the most abundant cell type in bone, are terminally differentiated osteoblasts that
68 have become buried in their own matrix. During this process, their morphology changes to stellate,
69 facilitating the formation of an extensive interconnected network throughout the bone matrix
70 termed the lacunar-canalicular network (LCN) [21-23]. Through the LCN, osteocytes sense
71 mechanical stimulus and translate them into biochemical signals, and appropriately control bone
72 homeostasis by regulating the function of both osteoclasts and osteoblasts. Therefore, the

73 osteocyte is now recognized as a major orchestrator of the bone remodeling process. However, the
74 understanding of the relationship between osteocytes and bone metastasis remains limited.

75 Bone metastasis is a multistage process. Long before the development of clinically detectable
76 metastases, circulating tumor cells settle and enter a dormant state in normal vascular and
77 endosteal niches present in the bone marrow, which provide immediate attachment and shelter,
78 and the cells only become active years later as they proliferate and alter the functions of
79 osteoclasts and osteoblasts, promoting skeletal destruction [24]. The endosteal niche, including
80 osteoblasts and osteoclasts, has been reported to provide tumor cells with an environment
81 supporting their survival and outgrowth, however, the role of osteocytes has been rarely addressed
82 [5]. Tumor cell dormancy is defined as an arrest in the cell cycle [25,26]. The details of niches and
83 signals that support tumor cell dormancy in bone metastasis are largely unknown. In the current
84 study, we discuss the effect of exercise on bone metastasis of NSCLC, and investigated the
85 potential effects and mechanisms of the osteocyte on the dormancy of bone metastasis NSCLC
86 cells.

87 ## Results

88 **Osteocytes inhibited NSCLC cell proliferation.**

89 To study the spatial distribution of NSCLC cell proliferation in bone metastasis, bone metastasis
90 tissues of six NSCLC patients were obtained. Bone destruction was found in the presence of bone
91 metastasis in NSCLC (Supplemental Figure 1a). Surprisingly, immunohistochemical staining
92 showed that Ki-67 was much lower in tumor cells adjacent to bone tissue than in the surrounding
93 tumor cells (Figure 1a). An intraosseous model was used to investigate the biological progression

94 of NSCLC cells in a bone microenvironment via direct tibial implantation of A549 in nude mice.
95 The results of biophotonic imaging, micro-CT, and hematoxylin and eosin (H&E) staining
96 indicated that the model was successfully established 21 days after modeling (Supplemental
97 Figure 1, b – d). Consistent with the result in the clinical samples, Ki-67 expression was much
98 lower in tumor cells adjacent to bone tissue than in the surrounding tumor cells (Figure 1b). The
99 above results indicated that NSCLC cells adjacent to bone tissue have a much lower proliferative
100 capacity than the surrounding tumor cells. Therefore, we hypothesized that bone tissues release
101 some substance that inhibits tumor growth.

102 To determine which type of cell inhibits proliferation after NSCLC cells have invaded bone
103 tissue, A549 was co-cultured with MLO-Y4, MC3T3-E1 and NCM460 (as a negative control)
104 cells for 48 h, respectively (Figure 1c). We found that the A549 migration ability was improved
105 after co-culture with MLO-Y4, with the promotional effect being much significantly stronger on
106 co-culture with MC3T3-E1 (Supplemental Figure 1e). More importantly, NSCLC cell
107 proliferation was inhibited after co-culture with MLO-Y4, whereas no inhibitory effect was found
108 after co-culture with MC3T3-E1 (Figure 1d, e and Supplemental Figure 1f), indicating that it is
109 osteocytes that inhibit NSCLC cell proliferation. Moreover, MLO-A5, another osteocyte-like cell,
110 also inhibited the proliferation of NSCLC cells (Supplemental Figure 1g). Surprisingly,
111 MC3T3-E1 proliferation was effectively enhanced on co-culture with MLO-Y4 (Figure 1f), which
112 indicated that the effect of osteocytes on NSCLC cell and osteoblast proliferation were different.
113 Taken together, these data suggested that it is osteocytes that inhibit NSCLC cell proliferation in
114 the endosteal niche.

115 **Osteocyte small extracellular vesicles inhibited NSCLC cell proliferation.**

116 To investigate the mechanism by which osteocytes inhibit NSCLC cell proliferation,
117 osteocyte-conditioned medium (CM) was separated into soluble factor (SF), large extracellular
118 vesicles (lEVs), and small extracellular vesicles (sEVs) fractions by serial ultracentrifugation and
119 ultrafiltration as performed previously with some modifications [27] (Figure 2a). The purified sEVs
120 were verified by transmission electron microscopy (TEM), NanoSight analysis, and
121 immunoblotting for protein markers (CD9, Alix, and TSG101), according to the proposal of the
122 International Society of Extracellular Vesicles (Supplemental Figure 2a – c). sEVs were labeled
123 with PKH67 and were observed to be internalized by NSCLC cells (Supplemental Figure 2d).
124 Subsequently, we treated the NSCLC cells with fractions derived from osteocyte CM, with
125 EV-depleted media as a negative control (fetal bovine serum [FBS] 10%). Interestingly, sEVs
126 from osteocyte CM had a much significantly greater potential to inhibit NSCLC cell proliferation
127 than the other groups (Supplemental Figure 2e, f), whereas sEVs from osteoblast CM had no
128 inhibitory effect on NSCLC cell proliferation (Figure 2 b, c).

129 To confirm the role of sEVs in osteocyte inhibition of NSCLC cell proliferation, GW4869 was
130 used to inhibit sEVs secretion. The significant reduction of sEVs released from MLO-Y4 on
131 GW4869 treatment was confirmed by NanoSight Analysis and western blotting (Figure 2d, e).
132 More importantly, it was found that GW4869 effectively eliminated the inhibitory effect of
133 MLO-Y4 on NSCLC cell proliferation (Figure 2f, g), which suggested that sEVs release was
134 required for osteocytes to inhibit NSCLC cell proliferation. Due to the complexity of the bone
135 marrow microenvironment, we examined the effect of bone marrow-derived sEVs on NSCLC
136 cells proliferation by CCK-8 assay. The results showed that bone marrow-derived sEVs could
137 promote the proliferation of NSCLC cells (Supplemental Figure 2g, h). Taken together, osteocytes

138 inhibit NSCLC cell proliferation by releasing sEVs.

139 **Osteocyte sEVs miR-99b-3p inhibited NSCLC cell proliferation by directly targeting murine**

140 **double minute2 (MDM2)**

141 Subsequently, we performed micro-RNA (miRNA) sequencing to investigate how

142 osteocyte-derived sEVs inhibit NSCLC cell proliferation. The miRNAs, which can be abundantly

143 encapsulated in sEVs, are key regulators of cancer cell proliferation. To identify the specific

144 miRNAs involved, we compared the miRNA profiles of MLO-Y4-sEVs and MC3T3-E1-sEVs,

145 the results of which are shown as heatmaps (Supplemental Figure 3a). Four of the maximally

146 upregulated miRNAs and two of the downregulated miRNAs were validated by real-time

147 quantitative polymerase chain reaction (qRT-PCR) (Figure. 3a).

148 These four upregulated miRNA sequences are identically conserved in the human and mouse.

149 To determine the effects of these miRNAs on NSCLC cell proliferation, A549 and NCI-H23 cells

150 were transfected with miRNA mimics or negative controls. We found that both miR-99b-3p and

151 miR-193a-5p significantly inhibited NSCLC cell proliferation 48 h after transfection (Figure 3b),

152 with miR-99b-3p having the most significant inhibitory effect. Inhibitors of miR-99b-3p, by

153 contrast, promoted NSCLC cell proliferation (Figure 3c, d). These data indicated that sEVs

154 released by osteocytes carried tumor suppressor miRNAs, such as miR-99b-3p.

155 Notably, in situ hybridization analysis demonstrated high miR-99b-3p expression in the cortical

156 bone of patients with bone metastases of NSCLC (Supplemental Figure 3b). To identify the

157 targets of miR-99b-3p, first, we applied PicTar and TargetScan to search for putative targets,

158 and > 100 mRNAs were predicted to be regulated by miR-99b-3p. Among these candidates, six

159 genes are involved in cell cycle or proliferation regulation. To determine whether miR-99b-3p

160 targets these genes directly, we cloned the 3'UTRs of the putative target into a dual luciferase
161 assay system. MDM2, as a negative regulator of p53, has been shown to exert oncogenic activity
162 [28]. A reporter assay using A549 cells revealed that miR-99b-3p significantly repressed MDM2
163 3'UTRs. Mutations of the putative miRNA sites in MDM2 3'UTRs abrogated the responsiveness
164 to miRNA (Figure 3e). Furthermore, transfection of miR-99b-3p mimicked reduced endogenous
165 MDM2 protein levels in A549 cells. By contrast, inhibition of miR-99b-3p significantly increased
166 the MDM2 protein level (Figure 3f).

167 Taken together, these results suggested that miR-99b-3p derived from osteocyte sEVs directly
168 down-regulates MDM2 expression through its 3'UTR, by which osteocytes inhibited NSCLC cell
169 proliferation.

170 **Mechanical stimulation increased osteocyte sEVs release and enhanced the inhibitory effect**
171 **of osteocytes on NSCLC cell proliferation**

172 Osteocytes are thought to be the principal mechanosensors of bone by translating mechanical
173 stimuli into molecular signals and appropriately controlling the downstream remodeling balance.
174 Exercise has the potential to improve physical function and the quality of life in individuals with
175 bone metastases. To determine whether osteocytes inhibit tumor proliferation by receiving
176 mechanical stimulation, MLO-Y4 cells were subjected to sinusoidal stretching at 12% strain at a
177 1.25 Hz frequency for 12 h, and sEVs were extracted from the CM. Interestingly, sEVs released
178 from mechanically-stimulated MLO-Y4 cells significantly inhibited NSCLC cell proliferation
179 compared to static osteocyte sEVs (Figure 4a, b and Supplemental Figure 4a, b). Moreover, the
180 mechanically-stimulated osteocytes sEVs had the most significant effect on the proliferation of
181 NSCLC cells compared with SF and lEVs components (Supplemental Figure 4c, d). Notably, the

182 concentration of sEVs of mechanically-stimulated osteocytes was much significantly higher than
183 that of static osteocyte sEVs (Figure 4c, d). Moreover, the miR-99b-3p content of osteocyte sEVs
184 increased significantly after stretching (Figure 4e).

185 To identify the effect of mechanical stimulation on bone metastasis of lung cancer in vivo,
186 mechanical loading (1 N at 2 Hz for 10 min per day, 5 days per week for four weeks) was applied
187 to the tibiae with bone metastasis induced by direct tibial implantation of GFP-LLC in mice. The
188 biophotonic imaging showed that tumor growth was inhibited by mechanical loading (Figure 4f).
189 Consistent with this, Ki-67 expression in NSCLC cells in the mechanical loading group was much
190 lower than that of the control group (Figure 4g). Dentin matrix protein 1 (DMP1), specifically
191 expressed in osteocytes, was used as a specific molecular marker of osteocytes in this study.
192 Meanwhile, CCND3 and GFP were selected for co-localization staining to confirm the above
193 phenomena, the results showed that mechanical loading could effectively inhibit tumor growth
194 (Supplemental Figure 4e). The micro-CT analysis of the proximal tibia showed that the
195 mechanical loading effectively protected bone integrity and delayed its destruction in the presence
196 bone metastasis in NSCLC, specifically reflected in the bone volume / total volume (BV/TV),
197 trabecular thickness (Tb.Th), and cortical thickness (Ct.Th) (Figure 4h and Supplemental Figure
198 4f). Furthermore, we found that AntagomiR-99b-3p could effectively rescue the inhibitory effect
199 on NSCLC cell proliferation, indicating that miR-99b-3p plays an important role in the
200 mechanically-inhibited proliferation of NSCLC cells (Figure 4i-k and Supplemental Figure 4g, h).
201 Taken together, these results suggested that mechanical stimulation enhanced the inhibitory effect
202 of osteocytes on bone metastasis progression by increasing the release of sEVs containing
203 proliferation-suppressive miRNA.

204 **Moderate exercise combined with zoledronic acid effectively suppressed bone metastasis**
205 **progression of NSCLC**

206 Exercise is one of the ways in which the body senses mechanical stress, so we evaluated the effect
207 of exercise in a mouse bone metastasis model. An intraosseous mouse model was used to
208 investigate the biological progression of NSCLC cells in a bone microenvironment by direct tibial
209 implantation of murine Lewis lung carcinoma (LLC) cells expressing green fluorescent protein
210 (GFP). These mice were subsequently randomized into tumor-bearing only (control), zoledronic
211 acid (ZA), treadmill running, and treadmill running combined with ZA (treadmill running+ZA)
212 groups. Moderate exercise was provided by treadmill running for mice, which were involuntarily
213 placed on a 12-lane rodent treadmill for 30 min per day at a speed of 15cm/s for at least 5 days per
214 week, and were euthanized after 4 weeks. Biophotonic imaging showed that tumor progression in
215 the three treated groups was significantly slower than that in the control group, among which, the
216 treadmill running+ZA group suppressed the growth of tumors in the tibia most effectively (Figure
217 5a). Tumor growth inhibition by the ZA and treadmill running groups was similar, with no
218 statistical difference. Ki-67 protein has been widely used as a proliferation marker for tumor cells.
219 In this study, immunofluorescence assessment results of Ki-67 and CCND3 were largely
220 consistent with those of biophotonic imaging (Figure 5b, Supplemental Figure 5). The Ki-67 and
221 CCND3 expression level was the lowest in the treadmill running+ZA group lung cancer cells in
222 the tibia, which confirmed that in the treadmill running+ZA group, tumor growth in the tibia was
223 suppressed most effectively. The micro-computed tomography (microCT) analysis showed that
224 treadmill running and/or ZA protected bone integrity and delayed bone destruction in the presence
225 of bone metastasis in NSCLC, among which, the treadmill running+ZA group displayed the

226 strongest effect, specifically reflected in the BV/TV, Tb.Th and Ct.Th (Figure 5c–e). The
227 protective effect of bone integrity in the ZA and treadmill running groups was similar, with no
228 statistical difference. Taken together, these results demonstrated that moderate exercise
229 significantly suppressed bone metastasis progression of NSCLC. Furthermore, moderate exercise
230 combined with ZA displayed additive effects.

231 **Exercise preconditioning effectively suppressed bone metastasis progression of NSCLC**

232 Physical exercise offers therapeutic potentials for bone metastasis. However, it remains mostly
233 unknown whether and how exercise preconditioning affects bone metastasis progression. In this
234 study, we examined the effects of preconditioning on bone metastasis progression in mature adult
235 mice using treadmill running. Male, 8-week-old C57BL/6J mice were subjected to 4 weeks of
236 treadmill exercise followed by tibial implantation of NSCLC cells. Mice were randomized into
237 tumor-bearing only (control), treadmill running before and after tibial implantation of NSCLC
238 cells (exercise preconditioning), and treadmill running after tibial implantation of NSCLC cells
239 (treadmill running) groups (Supplemental Figure 6a). The biophotonic imaging showed that tumor
240 growth in the two exercise groups was significantly slower than that in the control group, with the
241 exercise preconditioning group suppressing the tumor growth more significantly effectively than
242 treadmill running only after tibial implantation of NSCLC cells, which were consistent in
243 C57BL/6J and nude mice (Figure 6a). Regarding the proliferation marker, the Ki-67 and CCND3
244 immunofluorescence assessment results were largely consistent with those of the biophotonic
245 imaging (Figure 6b, Supplemental Figure 6b). The Ki-67 and CCND3 expression level in NSCLC
246 cells in the exercise preconditioning group was much significantly lower than that in the other
247 groups, which indicated that exercise preconditioning could effectively inhibit tumor growth. The

248 micro-CT analysis showed that the exercise protected bone integrity and delayed bone destruction
249 in the presence of bone metastasis in NSCLC, with the exercise preconditioning group having a
250 stronger effect than the other group, specifically reflected in the BV/TV, Tb.Th, and Ct.Th (Figure
251 6c–e). The micro-CT analyses of C57BL/6 mice and nude mice were consistent. Therefore,
252 these results suggested that maintaining exercise habits may effectively prevent bone metastasis of
253 NSCLC.

254 **Discussion**

255 Although many preclinical and clinical studies have shown that exercise can inhibit bone
256 metastasis progression [11,15], the mechanism remains poorly understood. Clarifying the mechanism
257 of action is essential to determine optimal exercise programs, design appropriate combination
258 therapy with standard therapy regimens, or identify specific targets for new treatment. In this
259 study, we found that NSCLC cells adjacent to bone tissue had a much lower proliferative capacity
260 than the surrounding tumor cells, thus we hypothesized that bone tissues release some substance
261 that inhibits tumor growth and sustains tumor dormancy in bone metastasis. Next, we
262 demonstrated that osteocytes inhibit NSCLC cell proliferation by releasing sEVs containing tumor
263 suppressor miRNAs, such as miR-99b-3p. Meanwhile, both in vitro and in vivo experiments
264 demonstrated that mechanical loading stimulated osteocytes to release more sEVs and
265 miR-99b-3p to delay the progression of bone metastasis of NSCLC. In addition, we showed that
266 bone metastasis progression of NSCLC was inhibited by moderate exercise, and combinations
267 with ZA had additive effects. Furthermore, exercise preconditioning effectively suppressed bone
268 metastasis progression of NSCLC. Taken together, our work elucidated a mechanism for the
269 clinical observation that bone metastasis was inhibited by moderate exercise.

270 In bone metastasis, only a limited number of disseminated tumor cells survive following bone
271 colonization, and these are retained in a dormant state for prolonged periods through engagement
272 in specialized endosteal niches before becoming reactivated to form overt metastases [5]. Currently,
273 molecular mechanisms for tumor cell dormancy in the endosteal niche remain poorly understood,

274 representing both a challenge and an opportunity for therapeutic targeting [29]. Bone metastases
275 occur from a complex interplay between cancer cells and bone cells. Interestingly, here we found
276 that NSCLC cells adjacent to bone tissue have a much lower proliferative capacity than the
277 surrounding tumor cells. Therefore, we hypothesized that bone tissues release some substance that
278 inhibits tumor growth and sustains NSCLC cell dormancy in bone metastasis.

279 Osteoclast and osteoblast functions in bone metastases have been well characterized; however,
280 the role of osteocytes needs to be elucidated [30]. Osteocytes act as mechanosensors to control
281 responses to mechanical loading of the skeleton. For bone metastases, osteocytes may play a
282 pivotal role in the interaction between mechanical loading and SREs. Here we demonstrated that it
283 is osteocytes that inhibit NSCLC cell proliferation in the endosteal niche, but not osteoblasts.
284 Furthermore, we demonstrated that osteocytes inhibit NSCLC cell proliferation by releasing sEVs
285 containing tumor suppressor miRNAs, such as miR-99b-3p. Recent studies showed that
286 miR-99b-3p functions as a potential tumor suppressor in oral squamous cell carcinoma and gastric
287 cancer [31,32]. We found that osteocyte sEVs miR-99b-3p inhibited NSCLC cell proliferation by
288 directly targeting MDM2. As a negative regulator of the p53, the most extensively studied human
289 tumor suppressor, MDM2 has been shown to exert oncogenic activity [28]. To date, three regions of
290 interaction between MDM2 and p53 have been identified, by which MDM2 inhibits the binding of
291 p53 to the transcriptional machinery. MDM2 is significantly highly expressed in lung
292 adenocarcinoma tissues compared with adjacent tissues, and is regarded as a proto-oncogene [33,34].
293 Our findings identified MDM2 as a direct target of miR-99b-3p, emphasizing the crucial role of
294 miRNA in bone metastases. Interestingly, the miR-99b-3p content in osteocyte sEVs increased
295 dramatically after mechanical loading, suggesting that miR-99b-3p may play a role in the
296 inhibition of bone metastases by exercise.

297 SREs resulting from bone metastasis are a major clinical problem that significantly harm patient
298 outcomes, and are commonly considered an incurable consequence of terminal malignancies.
299 Bone metastases from lung cancer represent the majority of cases, followed by prostate cancer and
300 breast cancer [35]. A recent animal study showed that in vivo exercise was protective against
301 metastatic bone loss and inhibited breast cancer progression in bone [36]. However, there was no
302 report about the effect of exercise on bone metastasis of lung cancer until recently. In the present

303 study, we showed that bone metastasis progression in lung cancer was inhibited by exercise. More
304 interestingly, exercise preconditioning effectively suppressed bone metastasis progression of
305 NSCLC, suggesting that maintaining exercise habits affords protection against bone metastasis.
306 Bisphosphonates are the standard of care in patients with bone metastases. Our study
307 demonstrated that moderate exercise and ZA have additive effects.

308 Exercise is quite complex because it involves multiple organs of the body. The bone can sense
309 the mechanical stress stimulus in the process of exercise. Using in vivo models, mostly breast
310 cancer bone metastasis models, several studies suggested that mechanical stimulation of the tibia
311 can contribute to inhibiting bone metastatic colonization and cancer progression in bone [36,37].
312 Tibial compression has been used to stimulate bone formation and study the interplay between
313 mechanical stimuli and SREs. One study showed that moderate tibial loading, but not overloading,
314 protected adult murine bone from destruction by metastasized breast cancer [36]. Consistent with
315 this, our work showed that mechanical loading of the tibia inhibited bone metastasis progression
316 of NSCLC. Although many preclinical and clinical studies have shown that exercise can inhibit
317 cancer progression, the ideal mechanism of implementation remains to be determined. The
318 prescription of exercise for patients with cancer requires further research, including exercise type,
319 frequency, duration, intensity, and whether it is supervised [14,16]. Exercise has been underutilized in
320 patients with advanced cancer despite the benefits, particularly for those with bone metastases
321 because of concerns over skeletal complications [38,39]. Multiple studies showed that individuals
322 with NSCLC were engaged in significantly less physical activity than similar-aged healthy
323 individuals [40,41]. Exercise models such as running are more realistic for healthy people, but
324 mechanical loading such as tibial compression provides for isolating the impacts of mechanical
325 stimuli on bone tissue in the context of SREs, which are more effective and safer for patients with
326 advanced cancer. Previous studies have shown that either exercise or mechanical loading can lead
327 to increased bone mass, which may be another reason for the attenuated erosion of NSCLC cells
328 and deserves our further exploration [42].

329 In conclusion, our study provides new insights into understanding the mechanism underlying
330 exercise-afforded protection against bone metastasis progression. Bone metastasis progression of
331 NSCLC was inhibited by moderate exercise. Osteocytes, sensing mechanical stimulation

332 generated by exercise, inhibit the proliferation of NSCLC cells and sustain their dormancy by
333 releasing sEVs containing tumor-suppressive miRNAs (Figure 7). Understanding the mechanism
334 underlying tumor dormancy may provide the foundation for the development of strategies to
335 prevent dormant bone metastasis from emerging as overt bone metastasis.

336 Materials and Methods

337 Patients

338 Lung cancer patients with a diagnosis of bone metastases (six patients, radiologically confirmed)
339 were recruited by the Third Affiliated Hospital of Southern Medical University (Guangzhou,
340 China) from January 2020 to January 2021. All patients were fully informed of the study, and they
341 provided written consent prior to participation. Surgically resected bone metastatic tumor tissue
342 was collected from all patients. The obtained bone metastatic tumor tissue was trimmed to an
343 appropriate size and rapidly transferred to formalin solution for storage until processing. We
344 confirm that our study was compliant with the "Guidance of the Ministry of Science and
345 Technology (MOST) for the Review and Approval of Human Genetic Resources". Ethics
346 approval was granted by the Human Research Ethics Committee of the Third Affiliated Hospital
347 of Southern Medical University. The study was conducted in accordance with the principles and
348 guidelines of The Declaration of Helsinki.

349 Cell lines

350 A549, LLC, NCM460, MLO-A5 and MLO-Y4 cells were purchased from the American Type
351 Culture Collection (Rockville, MD, United States) and grown in dulbecco's modified eagle
352 medium (DMEM) (Invitrogen, Waltham, MA, United States) containing 10% FBS and 1%
353 penicillin and streptomycin. MC3T3-E1 cells were purchased from the American Type Culture

354 Collection and were cultured in α Minimum Essential Medium (α-MEM) (Invitrogen) with 10%
355 FBS and 1% penicillin and streptomycin. These cell lines were not authenticated after purchase
356 but routinely tested negative for mycoplasma contamination.

357 **Animal models**

358 All animal experimental protocols were approved by the Animal Care and Use Committee of the
359 Southern Medical University, Guangzhou, China. C57BL/6 and nude athymic mice were obtained
360 from the Experimental Animal Center of the Southern Medical University in Guangzhou, China.
361 Animal care was in accordance with the guidelines of the US National Institutes of Health and the
362 Chinese National Institute of Health. All surgical interventions were performed under anesthesia
363 with a mixture of 13.3% urethane and 0.5% chloralose (0.65 ml/100 g body weight). All efforts
364 were made to reduce the number of animals used and to minimize animal discomfort.

365 For in situ studies, 25×10^4 LLC cells or A549 cells were injected into the tibiae of 8-week-old
366 C57BL/6 mice or nude mice. In brief, 25×10^4 LLC cells and A549 cells suspended in
367 phosphate-buffered saline (PBS) were injected into the tibia of C57BL/6 mice and nude mice,
368 respectively. Mice were euthanized on day 21 for analyses, unless otherwise indicated. For
369 stress-induced experiments, after 2 days of recovery, tibiae loading was performed daily on the
370 tumor-inoculated tibiae. Using an ElectroForce device (Bose, Framingham, MA, United States),
371 the tibiae of the mask-anesthetized mice were given daily loads of 1 N (peak-to-peak) at 2 Hz for
372 10 min, 5 days per week for 4 weeks. The tibias of a subset of mice were injected with
373 AntagomiR-NC or AntagomiR-99b-3p (GenePharma, Shanghai, China, 3 nmol per tibia, once a
374 week for 3 weeks) after 2 days of recovery.

375 For zoledronic acid experiments, starting on day 3 after lung cancer cell transplantation, mice

376 were treated with subcutaneous injection of 100 μg/kg zoledronic acid (Novartis, Basel,
377 Switzerland) or saline (other groups) every 3 days for 3 weeks, after which they were euthanized.
378 For exercise experiments, exercised mice were involuntarily placed on a 12-lane rodent treadmill
379 for 30 min per day at a speed of 15 cm/s for at least 5 days per week unless otherwise stated.
380 During the 3 days prior to euthanasia, the exercising mice underwent obligatory exercise,
381 regardless of how many consecutive days they had previously exercised. Two days after surgery,
382 all mice except the control group began moderate exercise by treadmill running, whereby they
383 were involuntarily placed on a 12-lane rodent treadmill for 30 min per day at a speed of 15 cm/s
384 for at least 5 days per week, and were euthanized after 4 weeks. For exercise preconditioning,
385 mice were additionally subjected to 4 weeks of treadmill exercise prior to tibial implantation of
386 NSCLC cells. In the matched experiment, the control mice were placed on a stationary (0 cm/s)
387 treadmill for the same time duration as the experimental mice.

388 We examined the effects of preconditioning on bone metastasis progression in mature adult
389 mice using treadmill running. Male 8-week-old C57BL/6J mice were subjected to 4 weeks of
390 treadmill exercise followed by tibial implantation of NSCLC cells.

391 **Lung cancer cell preparation and in situ injection**

392 We used clones derived from the GFP-tagged LLC cells and A549 cells. The cells were
393 maintained in DMEM containing 10% FBS and 0.1 mg/ml penicillin-streptomycin at 37 °C under
394 5%–8% CO_2. Cells were passaged at 80%–90% confluence and re-plated at a 1:10 dilution, which
395 was approximately every 72 h. Before in situ injection, cells were trypsinized at 80%–90%
396 confluence with 0.15% trypsin / ethylene diamine tetraacetic acid (EDTA) (0.5% Gibco trypsin
397 EDTA diluted 1:2 in PBS). Cells were immediately removed from the plate with 10 ml ice-cold

398 DMEM containing 10% FBS, pipetted into a 15 ml conical tube, and centrifuged at 200 × g for 5
399 min. The pellet was resuspended in a 50 ml conical tube in 25 ml ice-cold PBS (without Ca or Mg)
400 and counted. This was centrifuged to re-pellet, and finally resuspend at 25 × 10^4 cells/10 μl in
401 ice-cold PBS.

402 The mice were anesthetized using a mixture of 13.3% urethane and 0.5% chloralose (0.65
403 mL/100 g body weight). Both legs were cleaned with 10% povidone/iodine swab/solution,
404 followed by ethanol, repeated twice. The skin was wetted with 70% ethanol to increase visibility
405 of the underlying patellar ligament, which should be visible as a distinct, thick, white line. While
406 firmly grasping the ankle/leg of the mouse, a 28g ½ needle was inserted under the patella, through
407 the middle of patellar ligament, and into the anterior intercondylar area in the top of the tibia. A
408 gentle, lateral movement of the needle was applied to ensure it was in tibia and passed through the
409 growth plate. The plunger was slowly depressed to inject 10 μl of cell solution. After 3 min, the
410 needle was slowly extracted. The treated mice were kept on a heating pad until revived.

411 **Mechanical stress stimulation of MLO-Y4 cells**

412 MLO-Y4 cells were transferred to a Biofex six-well plate (Flexcell, Burlington, NC, USA) and
413 allowed to adhere to the membrane until they attained 90% confluence. The cells were subjected
414 to sinusoidal stretching (Flexcell) at 12% strain and 1.25 Hz frequency for 12 h. Experiments were
415 performed at 37 °C under 5% CO_2. Following 48 h of stretching, the CM (or control medium) was
416 collected for sEVs extraction.

417 **Bio-photon imaging and micro-CT imaging**

418 Tumor-bearing mice were euthanized 30 days after tumor cell injection, and their hind limb bones
419 were imaged by biophotonics. Fluorescence imaging for GFP-labeled tumor cells in these bones

420 was performed using the optical imaging system, Fx Pro (Bruker BioSpin MRI GmbH, Ettlingen,
421 Germany). For anatomical orientation, a white light/grayscale picture was performed and used
422 with the fluorescent signal (Cy3.5: excitation = 570 nm; emission = 620 nm). For data analysis,
423 molecular imaging software 7.1.3 (Bruker BioSpin MRI GmbH) was used. Regions of interest
424 (ROIs) were defined around the bone and analyzed compared to the background of PBS injection
425 to calculate the signal to noise ratio.

426 Micro-CT was performed using the Skyscan 1172 (Bruker-MicroCT, Kontich, Belgium). The
427 X-Ray tube settings were 80 kV and 500 µA and images were acquired at the highest resolution
428 without charge coupled device binning, resulting in a voxel size of 9.44 µm. A 0.66° rotation step
429 through a 195° angular range with 6500 msec exposure was used. After processing with a
430 three-dimensional Gaussian filter to reduce noise, the ROIs were manually segmented such that
431 they corresponded to the cortical and trabecular bone regions. Cortical ROIs comprised 470 µm
432 thick regions (50 slices, 9.4 µm thickness per slice) located 3 mm distal to the growth plate, while
433 300 µm thick trabecular sections began 0.27 mm distal to the growth plate.

434 **Histological analysis, immunohistochemistry, and immunofluorescence staining**

435 Bone samples were fixed in 4% paraformaldehyde in PBS and decalcified in a 10% EDTA
436 solution. They were subsequently dehydrated through a series of graded alcohols, cleared in
437 xylene, and embedded in paraffin. Sagittal sections of 2–5 µm were prepared for histological
438 analyses. Following deparaffinization and rehydration, H&E staining were performed on the tissue
439 sections. The tissue sections were imaged using an FSX100 microscope (Olympus, Tokyo, Japan).

440 For immunohistochemistry, sections were incubated in 10 mM citrate buffer (pH 6.0) for 30
441 min at 90 °C or treated with 200 mg/mL proteinase K (Sigma Aldrich, St. Louis, MO, United

442 States) for 10 min at 37 °C to unmask antigen. Subsequently, the sections were treated with 3%
443 hydrogen peroxide for 15 min. Thereafter, the sections were permeabilized with 0.1% Triton
444 X-100 in PBS for 5 min at room temperature and blocked with 1% sheep serum at room
445 temperature for 1 h. We incubated the sections with a primary antibody that recognized Ki67 (Cell
446 Signaling Technology, Danvers, MA, United States, cat. #: 9129, 1:200) overnight at 4 °C.
447 Subsequently, we used a horse radish peroxidase-labeled secondary antibodies (1:200 in 1%
448 bovine serum albumin [BSA], 1 h) at 37°C. Diaminobenzidine was used as a chromogen and
449 hematoxylin as the counterstain.

450 For immunofluorescence, we incubated primary antibodies that recognized Ki67 (Cell
451 Signaling Technology, cat. #: 9129, 1:200), DMP1 (R&D Systems, Minneapolis, MN, United
452 States, cat. #: AF4386, 1:100), GFP (ABclonal, Wuhan, China, cat. #:AE012, 1:100) and CCND3
453 (Bioss, Woburn, MA, United States, cat. #: bs-0660R, 1:100) overnight at 4 °C. For secondary
454 reactions, species-matched Alexa Fluor 488- and Alexa Fluor 594-secondary antibodies were used
455 (1:500 in 1% BSA, 1 hour) at 37 °C in the dark. The secondary antibodies for
456 immunofluorescence staining were goat anti-rabbit Alexa Fluor 488 (Invitrogen, cat#A-11008)
457 and donkey anti-Sheep Alexa Fluor 594 (Invitrogen, cat#A-11016). The sections were mounted
458 with 4',6-diamidino-2-phenylindole (DAPI) (Thermo Fisher, Waltham, MA, United States) before
459 imaging and we examined more than five different microscopic images (per section) under a
460 confocal laser scanning microscope (Olympus, Tokyo, Japan).

461 **In situ hybridization.**

462 In situ hybridization was performed to determine the expression of miR-99b-3p using miRCURY
463 LNA miRNA Detection, Optimization Kit 2 (miR-99b-3p) (Exiqon, Vedbæk, Denmark),

464 according to the manufacturer's protocol. Sections were serially cut to 4 μm thicknesses, the
465 tissues were subjected to pepsin (1.3 mg/mL, Sigma Aldrich) for 30 min. After washing in PBS,
466 the slides were submerged in 99.7% ethanol and air-dried. Slides were hybridized with 40 nM
467 miR-99b-3p in an incubation chamber at 37℃ for 16 – 18 h, followed by stringent washes with
468 saline-sodium citrate buffer at 37℃. For immunodetection, slides were blocked with digoxigenin
469 blocking reagent (Roche, Mannheim, Germany) in maleic acid buffer containing 2% sheep serum
470 at ambient temperature for 60 min and then incubated with sheep anti-digoxigenin conjugated to
471 ALP (diluted 1:800 in blocking reagent) at ambient temperature for 60 min, resulting in dark-blue
472 staining. The NBT/BCIP reaction mixture1 was incubated within a humidified chamber at 37℃
473 for 2 h and the reaction was stopped with KTBT buffer, and then washed in PBS three times,
474 dehydrated, and mounted for microscopy.

475 **Western blot analysis.**

476 Cells and sEVs were lysed with 2% Sodium dodecyl sulfonate (SDS), 2 M urea, 10% glycerol, 10
477 mM Tris-HCl (pH 6.8), 10 mM dithiothreitol, and 1 mM phenylmethylsulfonyl fluoride. The
478 lysates were separated by SDS-polyacrylamide gel electrophoresis and blocked with BSA.
479 Following blotting onto a nitrocellulose membrane (Bio-Rad Laboratories, Hercules, CA, United
480 States), the membrane was incubated with primary antibodies that recognized TSG101 (Abcam,
481 Cambridge, United Kingdom cat. #: ab83, 1:1,000), CD63 (Abcam, cat. #: ab193349, 1:1,000),
482 CD9 (Abcam, cat. #: ab223052, 1:1,000), Alix (Abcam, cat. #: ab76608, 1:1,000), β-actin (Cell
483 Signaling Technology, cat. #: 4970S, 1:4000), MDM2 (Proteintech, Wuhan, China cat. #:
484 66511-1-IG, 1:1000), and GAPDH (Cell Signaling Technology, cat. #: 2118, 1:5000) overnight at
485 4 °C. Secondary antibodies for western blot were anti-rabbit IgG, (cat# 7074, dilution 1:2000)

486 from Cell Signaling Technology and anti-mouse IgG, (cat# A9044, dilution 1:2000) from Sigma
487 Aldrich (1 hour at 37 °C). The membrane was analyzed using specific antibodies and visualized
488 using an enhanced chemiluminescence 50 kit (Amersham Biosciences, Piscataway, NJ, United
489 States).

490 **Transwell assay.**

491 The migration capacity of cancer cells was determined using a 24-well plate, Transwell chambers
492 (Thermo Fisher) with an 8-μm pore size, and Matrigel (100 $\mu g \cdot mL^{-1}$). Approximately 5×10^4
493 cells in 200 μL serum-free DMEM were plated in the upper chambers, and 800 μL CM was added
494 to the lower chambers. After 48 h, the cells that had invaded to the lower side of the membrane
495 were stained with crystal violet. At minimum of five randomly selected images were acquired, and
496 the mean number of stained cells was determined.

497 **Luciferase assays.**

498 A549 cells were cultured at 1×10^5 cells/well in 12-well plates. The cells were co-transfected with
499 miR-99b-3p mimic (50 nM) or miRNA mimic negative control (50 nM) and 0.2 μg
500 psiCHECK™-1-UTR. Transfection was performed using Lipofectamine 3000. After 48 h, cells
501 were collected and luciferase activity was determined using the DualLuciferase reporter assay
502 system (Promega, Madison, WI, United States) with the dual luciferase assay reporter-ready
503 luminometer (Promega). The assays were performed in triplicate.

504 **TEM and nanosight tracking analysis.**

505 The morphology of the sEVs was observed by TEM. Briefly, the sEVs suspension was mixed with
506 an equal amount of 4% paraformaldehyde. Following washing with PBS, 4% uranyl acetate was
507 added for chemical staining of sEVs, and images were captured using a Hitachi H-7650 TEM

508 (Hitachi, Tokyo, Japan). Nanosight tracking analysis was performed to determine the size and
509 concentration of the isolated sEVs using the NanoSight NS500 (Malvern, Westborough, MA,
510 United States), according to the operating instructions, without any changes. The sEVs were
511 diluted to be within the recommended concentration range. Five 60 s videos were captured for
512 each sample during flow mode (camera settings: slider shutter 890, slider gain 146). SEVs were
513 diluted and loaded onto the NS500 instrument by a syringe. The videos were analyzed with the
514 NTA 3.2 software (Malvern). All measurements were performed at room temperature.

515 **RNA isolation**

516 RNA was extracted from cells using the QIAzol Lysis Reagent (Qiagen, Hilden, Germany)
517 according to the user guidelines. Briefly, cells were collected in a reaction tube, lysed with QIAzol,
518 and mixed with chloroform. Following centrifugation at 12,000 × g for 15 min at 4 °C, the upper
519 aqueous phase was transferred to an RNeasy Mini spin column in a 2 mL collection tube and
520 mixed with 100% ethanol. Following washing at 7500 × g for 5 min at 4 °C, the total RNA was
521 collected for qRT-PCR analysis. RNA was extracted from sEVs fractions using the Qiagen
522 miRNeasy Mini kit (Qiagen) according to the manufacturer's instructions, with a final elution
523 volume of 50 μL.

524 **MiRNA sequencing**

525 Total RNA extraction from the samples was conducted using the miRNeasy Kit (Qiagen),
526 according to standard operating procedures provided by the manufacturer. The quality and
527 integrity of the total RNA were determined using the Agilent 2100 Bioanalyzer and the RNA 6000
528 Nano LabChip Kit (Agilent, Santa Clara, CA, United States). A sequencing RNA library was
529 constructed by performing a 3′-end linker, a 5′-end linker, reverse transcription, amplification,

530 cDNA library size selection, and purification steps using total RNA. Cluster generation and first
531 stage sequencing primer hybridization were performed on the cBot of the Illumina HiSeq
532 sequencer from Shanghai Biotechnology (Shanghai, China), according to the corresponding
533 procedure in the cBot User Guide. Subsequently, the sequencing reagent was prepared following
534 the Illumina User Guide and the flow cell carrying the cluster was loaded into the machine.
535 Single-end sequencing was performed using the single-read program. The sequencing process was
536 controlled by the data collection software provided by Illumina that performed real-time data
537 analyses.

538 **RT-PCR and qRT-PCR**

539 RNA samples were quantitated and qualified using a NanoDrop analyzer (ThermoFisher). Equal
540 quantities (5 ng) of total RNA from each sample were used for cDNA synthesis using the
541 PrimeScript®RT reagent kit (TaKaRa, Tokyo, Japan). The reverse transcriptions of miRNAs were
542 performed using looped miRNA-specific RT primers for miRNAs. qRT-PCR was performed with
543 the Step One Plus (Applied Biosystems, Carlsbad, CA, United States, using an SYBR Green I
544 Real-Time PCR Kit (GenePharma) for miR-99b-3p. Dissociation curves were generated to ensure
545 the specificity of each qRT-PCR reaction. The relative expression levels of miRNAs in each
546 sample were calculated and quantified using the $2^{-\Delta\Delta CT}$ method after normalization for expression
547 of the positive control.

548 **Co-culture experiments**

549 Well inserts with a 0.4 mm pore size filter (BD Falcon, Franklin Lake, NJ, United States) for
550 six-well plates were used following the manufacturer's instructions. MLO-Y4 and MC3T3-E1
551 cells were seeded into the well inserts (5×10^5 cells/well) with DMEM medium. LLC, A549, and

552 MLO-Y4 cells were also seeded into six-well plates (1×10^6 cells/well). After 48h of co-culture,
553 cells in 6-well plates were subjected to the next experiments. All co-culture experiments were
554 conducted in DMEM with sEVs-free FBS (Life Technologies, Carlsbad, CA, United States).

555 **Differential ultracentrifugation of several fractions from CM and sEVs isolation**

556 To isolate the different CM fractions, 1×10^6 cells were plated in a 10 cm dish (10 ml medium).
557 After 72 h we either separated the conditioned media or isolated sEVs. For isolated bone
558 marrow-derived sEVs, suspensions were obtained by flushing mouse bone marrow with medium.
559 The supernatant was aspirated after settling, and impurities and cells from the bone marrow were
560 removed by centrifugation (300 × g for 5 min and 600 × g for 10 min, subsequent steps were
561 performed as for CM). For the dissection of the CM, whole CM (10 ml for one 10 cm dish) was
562 collected by pipetting from the 10 cm dish into 50 mL falcon tubes, centrifuged at low speed
563 (2,000 × g for 20 min) to eliminate dead cells and cellular debris prior to use, and divided into two.
564 One half was used as whole CM, concentrated with a 10 KD ultrafiltration device (Millipore,
565 Billerica, MA, United States) at 5000 × g for 15 min and were transferred to 12 wells of a 96-well
566 plate, while the remaining half was further processed. From the second half, lEVs were collected
567 after a 10,000 × g centrifugation step for 1 h, washed in 15 mL PBS, and centrifuged again at
568 10,000 × g for 1 h. The SF was filtered through a 0.22 mm filter prior to a 100,000 × g
569 centrifugation step. The SF was collected after a 80 min 100,000 × g centrifugation step and
570 concentrated using a 10 KD ultrafiltration device (Millipore) at 5000 × g for 15 min, obtaining
571 concentrated factor. The final 100,000 × g pellet (sEVs) was washed once in 15 ml PBS and
572 resuspended in 10% EV-depleted FBS medium for the functional cell culture experiments. Each
573 individual SF, lEVs, and sEVs fraction was used were transferred to 12 wells of a 96-well plate.

574 SEVs from 10 ml of conditioned media were added either to 6 wells of a 96-well plate or one well
575 of a 12-well plate. Media with EV-depleted serum (10% FBS) was used as a negative control in
576 most experiments.

577 **Cell counting kit-8 assay**

578 The Cell Counting Kit-8 assay (CCK-8) was used to determine cell viability. In total, 2×10^3 cells
579 were seeded in 96-well plates and allowed to adhere overnight. Following incubation with the
580 compounds under evaluation for 24h, 48h, 72 h and 96h (the bar chart shows the results at 72 h) ,
581 10 μL CCK-8 dye was added to each well, and the cells were incubated for 1 h at 37 °C.
582 Subsequently, the absorbance was determined at 450 nm (BioTek Synergy-HTX, Winooski, VT,
583 United States).

584 **Flow cytometry**

585 Approximately 10,000 cells were seeded in 12-well plates on day 1. Treatment was added on day
586 2, and cell proliferation was examined using a fluorescence-based cell proliferation kit (Cell-Light
587 EdU Apollo488 In Vitro Flow Cytometry Kit, Ribobio, Guangzhou, China) on day 4. Following
588 fluorescence labeling, the ratio of the number of fluorescently labeled cells to the total number of
589 cells was determined by flow cytometry (Beckman, Brea, CA, United States).

590 **SEVs labeling and cellular uptake**

591 SEVs were labeled using the PKH67 Green Fluorescent Cell Linker Kit (Sigma-Aldrich) by
592 following the manufacturer's protocol. The isolated sEVs diluted in PBS was added to 0.5 mL
593 Diluent C. Subsequently, 2 μL PKH67 dye was added and incubated for 4 min at room
594 temperature. Two milliliters of 1% BSA/PBS was added to bind excess dye. The labeled sEVs
595 were washed at 100,000 × g for 70 min, and the sEVs pellet was suspended in PBS and used for

596 uptake experiments. We subsequently co-cultured these PKH67 sEVs with A549. After the
597 indicated time of co-culture, we stained the A549 with DAPI (Sigma-Aldrich) and observed them
598 by confocal microscopy.

599 **Statistical analysis**

600 All data were analyzed for statistical significance using GraphPad Prism 6.0 software (GraphPad
601 Software, San Diego, CA, United States). The P value was determined by the Student's t-test for
602 two-group, or one-way analysis of variance test for multiple group comparisons. It was considered
603 indicative of statistical significance when $P < 0.05$. All experiments were repeated a minimum of
604 three times. Quantitative data were expressed as mean ± standard error of the mean.

605 **Data availability statement**

606 All data generated or analyzed during this study are included in this submitted article and its
607 additional files.

608 **Author contributions**

609 QCS and XCB designed the experiments. JX, YFX, XHL, LL, and JC performed the experiments
610 and analyzed the data. QCS, XCB, and JX wrote the original manuscript. YS, RXZ, and JRL
611 assisted with cell culture and in vivo experiments. YFX, ZQC, and ZMZ assisted with the
612 collection of patient samples and editing of the manuscript. QCS, JX and CYH supplemented the
613 experiments and revised the manuscript. All authors contributed to the article and approved the
614 submitted version.

615 **Acknowledgments**

We thank the Central Laboratory, Southern Medical University for providing facilities and technical support. This work was supported by grants from the National Natural Science Foundation of China (Grant No. 81991511 and No. 82202930).

Competing interests

The authors have declared that no conflict of interest exists.

References

1. Sung, H., *et al.* Global cancer statistics 2020: GLOBOCAN estimates of incidence and mortality worldwide for 36 cancers in 185 countries. *Ca-a Cancer Journal for Clinicians* **71**, 209-249 (2021).
2. Herbst, R.S., Morgensztern, D. & Boshoff, C. The biology and management of non-small cell lung cancer. *Nature* **553**, 446-454 (2018).
3. Cetin, K., Christiansen, C.F., Jacobsen, J.B., Norgaard, M. & Sorensen, H.T. Bone metastasis, skeletal-related events, and mortality in lung cancer patients: a Danish population-based cohort study. *Lung Cancer* **86**, 247-254 (2014).
4. Riihimaki, M., *et al.* Metastatic sites and survival in lung cancer. *Lung Cancer* **86**, 78-84 (2014).
5. Zhang, W.J., Bado, I., Wang, H., Lo, H.C. & Zhang, X.H.F. Bone Metastasis: Find Your Niche and Fit in. *Trends in Cancer* **5**, 95-110 (2019).
6. Sowder, M.E. & Johnson, R.W. Bone as a Preferential Site for Metastasis. *JBMR plus* **3**, e10126 (2019).
7. Knapp, B.J., Devarakonda, S. & Govindan, R. Bone metastases in non-small cell lung cancer: a narrative review. *J Thorac Dis* **14**, 1696-1712 (2022).
8. Pedersen, L., *et al.* Voluntary Running Suppresses Tumor Growth through Epinephrine- and IL-6-Dependent NK Cell Mobilization and Redistribution. *Cell Metab* **23**, 554-562 (2016).
9. Schmitz, K.H., *et al.* Exercise is medicine in oncology: Engaging clinicians to help patients move through cancer. *CA: a cancer journal for clinicians* **69**, 468-484 (2019).
10. Bade, B.C., Thomas, D.D., Scott, J.B. & Silvestri, G.A. Increasing physical activity and exercise in lung cancer: reviewing safety, benefits, and application. *J Thorac Oncol* **10**, 861-871 (2015).
11. Ligibel, J.A., *et al.* Exercise, Diet, and Weight Management During Cancer Treatment: ASCO Guideline. *J Clin Oncol* **40**, 2491-2507 (2022).
12. Kerr, J., Anderson, C. & Lippman, S.M. Physical activity, sedentary behaviour, diet, and cancer: an update and emerging new evidence. *Lancet Oncol* **18**, e457-e471 (2017).
13. Cao, C., Friedenreich, C.M. & Yang, L. Association of Daily Sitting Time and Leisure-Time Physical Activity With Survival Among US Cancer Survivors. *JAMA Oncol* **8**, 395-403 (2022).

14. Stout, N.L., Santa Mina, D., Lyons, K.D., Robb, K. & Silver, J.K. A systematic review of rehabilitation and exercise recommendations in oncology guidelines. *CA Cancer J Clin* **71**, 149-175 (2021).
15. Weller, S.*, et al.* Exercise for individuals with bone metastases: A systematic review. *Crit Rev Oncol Hematol* **166**, 103433 (2021).
16. Cavalheri, V. & Granger, C.L. Exercise training as part of lung cancer therapy. *Respirology* **25**, 80-87 (2020).
17. Wang, Q.Y. & Zhou, W.L. Roles and molecular mechanisms of physical exercise in cancer prevention and treatment. *J Sport Health Sci* **10**, 201-210 (2021).
18. Zhu, C.M.*, et al.* Exercise in cancer prevention and anticancer therapy: Efficacy, molecular mechanisms and clinical information. *Cancer Letters* **544**(2022).
19. Ruiz-Casado, A.*, et al.* Exercise and the Hallmarks of Cancer. *Trends in Cancer* **3**, 423-441 (2017).
20. Wang, L.J., You, X.L., Zhang, L.L., Zhang, C.Q. & Zou, W.G. Mechanical regulation of bone remodeling. *Bone Research* **10**(2022).
21. Prideaux, M., Findlay, D.M. & Atkins, G.J. Osteocytes: The master cells in bone remodelling. *Curr Opin Pharmacol* **28**, 24-30 (2016).
22. Schaffler, M.B., Cheung, W.Y., Majeska, R. & Kennedy, O. Osteocytes: master orchestrators of bone. *Calcif Tissue Int* **94**, 5-24 (2014).
23. Robling, A.G. & Bonewald, L.F. The Osteocyte: New Insights. in *Annual Review of Physiology, Vol 82*, Vol. 82 (eds. Nelson, M.T. & Walsh, K.) 485-506 (2020).
24. Clezardin, P.*, et al.* Bone metastasis: mechanisms, therapies, and biomarkers. *Physiol Rev* **101**, 797-855 (2021).
25. Phan, T.G. & Croucher, P.I. The dormant cancer cell life cycle. *Nature Reviews Cancer* **20**, 398-411 (2020).
26. Blasco, M.T., Espuny, I. & Gomis, R.R. Ecology and evolution of dormant metastasis. *Trends in Cancer* **8**, 570-582 (2022).
27. Fafian-Labora, J.A., Rodriguez-Navarro, J.A. & O'Loghlen, A. Small Extracellular Vesicles Have GST Activity and Ameliorate Senescence-Related Tissue Damage. *Cell Metab* **32**, 71-+ (2020).
28. Karni-Schmidt, O., Lokshin, M. & Prives, C. The Roles of MDM2 and MDMX in Cancer. *Annual review of pathology* **11**, 617-644 (2016).
29. Clezardin, P.*, et al.* Bonemetastasis: Mechanisms, Therapies, and Biomarkers. *Physiological Reviews* **101**, 797-855 (2021).
30. Atkinson, E.G. & Delgado-Calle, J. The Emerging Role of Osteocytes in Cancer in Bone. *JBMR plus* **3**, e10186 (2019).
31. He, K.*, et al.* miRNA-99b-3p functions as a potential tumor suppressor by targeting glycogen synthase kinase-3 beta in oral squamous cell carcinoma Tca-8113 cells. *Int J Oncol* **47**, 1528-1536 (2015).
32. Chang, S.E.*, et al.* miR-99b-3p is induced by vitamin D3 and contributes to its antiproliferative effects in gastric cancer cells by targeting HoxD3. *Biol Chem* **400**, 1079-1086 (2019).
33. Ni, L.W.*, et al.* MiR-221-3p-mediated downregulation of MDM2 reverses the paclitaxel resistance of non-small cell lung cancer in vitro and in vivo. *Eur J Pharmacol* **899**(2021).

697 34. Chen, B., *et al.* SHANK1 facilitates non-small cell lung cancer processes through
698 modulating the ubiquitination of Klotho by interacting with MDM2. *Cell Death Dis*
699 **13**(2022).
700 35. Ryan, C., *et al.* Epidemiology of bone metastases. *Bone* **158**(2022).
701 36. Wang, S., *et al.* Moderate tibial loading and treadmill running, but not overloading,
702 protect adult murine bone from destruction by metastasized breast cancer. *Bone* **153**,
703 116100 (2021).
704 37. Fan, Y., *et al.* Skeletal loading regulates breast cancer-associated osteolysis in a loading
705 intensity-dependent fashion. *Bone Res* **8**, 9 (2020).
706 38. Cheville, A.L., Kornblith, A.B. & Basford, J.R. An examination of the causes for the
707 underutilization of rehabilitation services among people with advanced cancer. *Am J*
708 *Phys Med Rehabil* **90**, S27-37 (2011).
709 39. Ten Tusscher, M.R., *et al.* Education Needs of Dutch Physical Therapists for the Treatment
710 of Patients With Advanced Cancer: A Mixed Methods Study. *Phys Ther* **100**, 477-486
711 (2020).
712 40. Granger, C.L., Denehy, L., McDonald, C.F., Irving, L. & Clark, R.A. Physical activity
713 measured using global positioning system tracking in non-small cell lung cancer: an
714 observational study. *Integr Cancer Ther* **13**, 482-492 (2014).
715 41. Granger, C.L., *et al.* Low physical activity levels and functional decline in individuals with
716 lung cancer. *Lung Cancer* **83**, 292-299 (2014).
717 42. Robling, A.G., Castillo, A.B. & Turner, C.H. Biomechanical and molecular regulation of
718 bone remodeling. *Annu Rev Biomed Eng* **8**, 455-498 (2006).

Figures

Figure 1

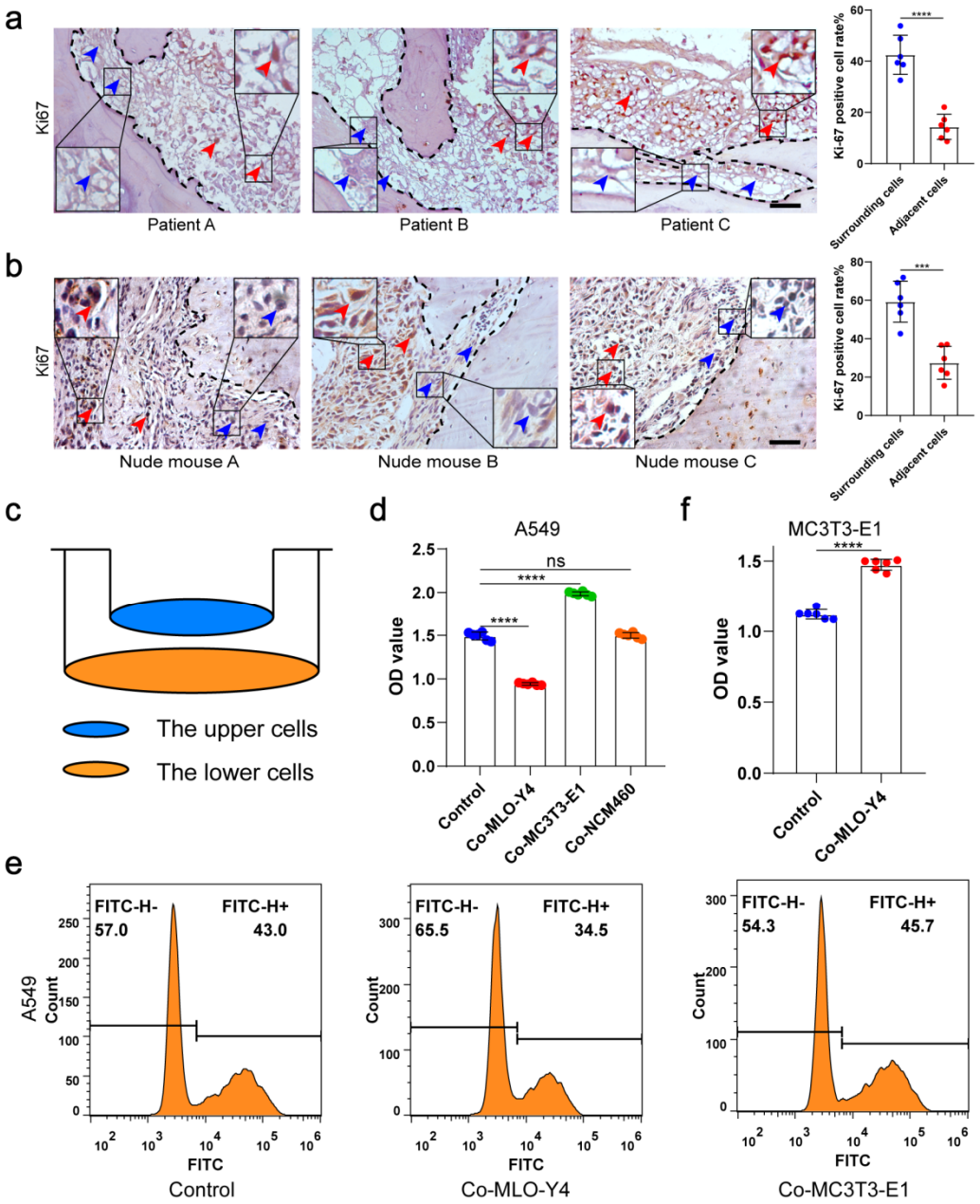

721 **Figure 1. Osteocytes inhibited the proliferation of NSCLC cells.**

722 a. Representative immunohistochemical staining and quantification of Ki-67 in bone metastasis
723 site of patients with NSCLC. The dashed line indicates the boundary between bone and tumor.
724 Scale bars: 50 μm. Blue arrows, low expression or negative of Ki67. Red arrows, high expression
725 of Ki67. Tumor cells ≤50 μ m from bone tissue were defined as adjacent cells, and those > 50 μ
726 m from bone tissue were defined as surrounding cells. n=6; Student's two-sided unpaired t test.

727 b. An intraosseous model of bone metastasis was used via direct implantation of NSCLC cells
728 A549 into tibia of nude mice. Three weeks after implantation, mice were sacrificed.
729 Representative immunohistochemical staining and quantification of Ki-67 in tibia of
730 tumor-bearing nude mice. The dashed line indicates the boundary between bone and tumor. Scale
731 bars: 50 μm. Blue arrows, low expression or negative of Ki67. Red arrows, high expression of
732 Ki67. Tumor cells ≤50 μ m from bone tissue were defined as adjacent cells, and those > 50 μ m
733 from bone tissue were defined as surrounding cells. n=6; Student's two-sided unpaired t test.

734 c. Schematic diagram of co-culture.

735 d. CCK-8 assays were performed to evaluate the effects of MLO-Y4 cells, MC3T3-E1 or
736 NCM460 cells on the proliferation of A549 cells in the co-culture system. n=6; one-way analysis
737 of variance with Turkey's multiple comparisons test.

738 e. EdU flow cytometry were performed to evaluate the effect of MLO-Y4 cells on the proliferation
739 of A549 cells in the co-culture system.

740 f. CCK-8 assays were performed to evaluate the effect of MLO-Y4 cells on the proliferation of
741 MC3T3-E1 cells in the co-culture system. n=6; Student's two-sided unpaired t test.

742 no significance (ns) P>0.05, *P < 0.05, **P < 0.01, ***P < 0.001, ****P < 0.0001.

743 **Figure 2**

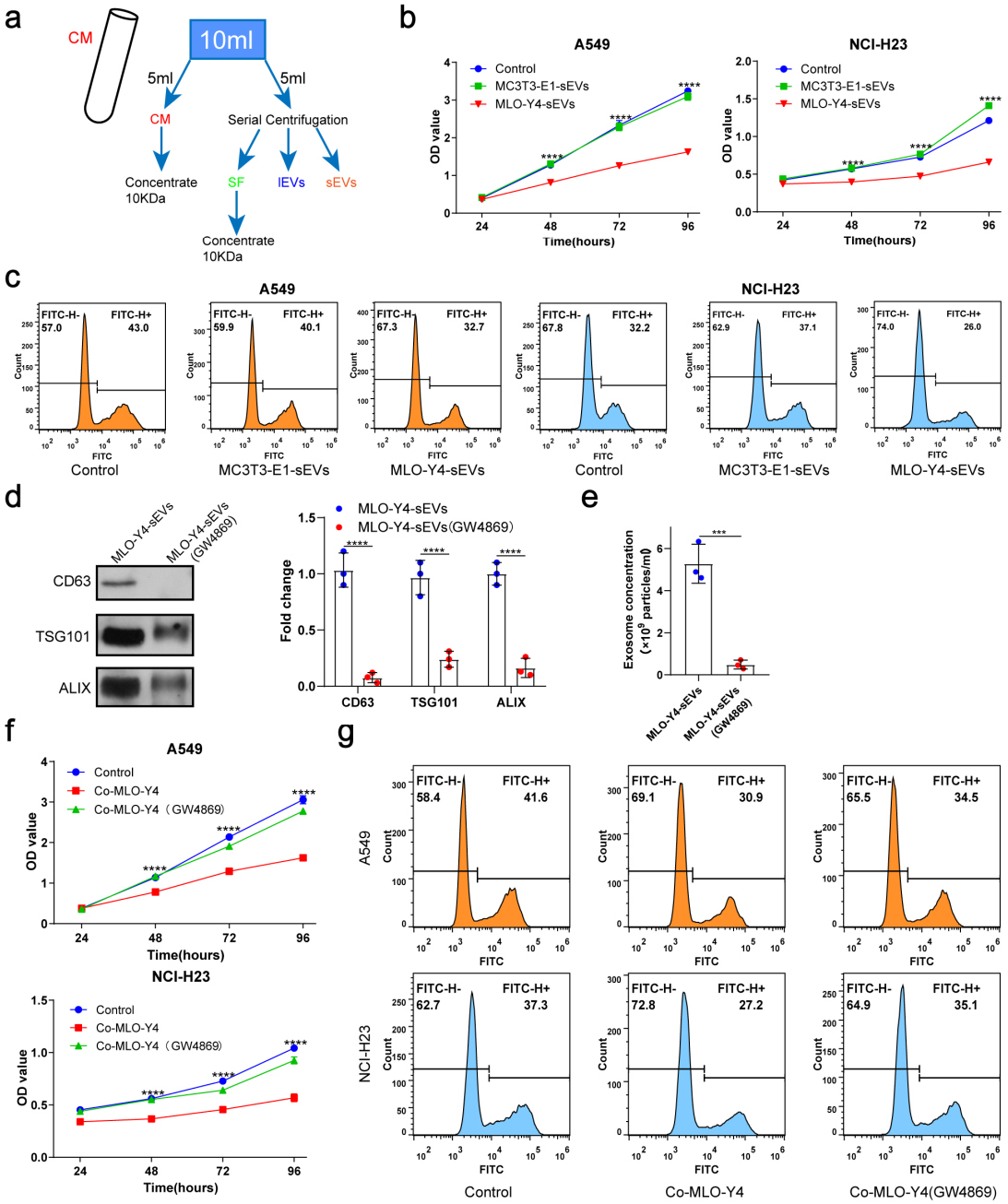
a
CM
10ml
5ml
5ml
CM
Serial Centrifugation
Concentrate
10KDa
SF
IEVs
sEVs
Concentrate
10KDa
b
A549
NCI-H23
Control
MC3T3-E1-sEVs
MLO-Y4-sEVs
OD value
Time(hours)
c
A549
NCI-H23
FITC-H-
FITC-H+
Count
FITC
Control
MC3T3-E1-sEVs
MLO-Y4-sEVs
d
MLO-Y4-sEVs
MLO-Y4-sEVs (GW4869)
CD63
TSG101
ALIX
Fold change
e
Exosome concentration (×10^9 particles/ml)
f
A549
NCI-H23
Control
Co-MLO-Y4
Co-MLO-Y4（GW4869）
OD value
Time(hours)
g
A549
NCI-H23
Control
Co-MLO-Y4
Co-MLO-Y4(GW4869)

744 **Figure 2. Osteocyte sEVs inhibited the proliferation of NSCLC cells.**

745 a. Schematic diagram of serial centrifugation and concentration of culture medium. Conditioned
746 medium (CM) was separated into soluble factor (SF), large extracellular vesicles (lEVs), and
747 small extracellular vesicles (sEVs) fractions, by serial ultracentrifugation and ultrafiltration.

748 b. CCK-8 assays were performed to evaluate the effect of sEVs on the proliferation of NSCLC
749 cells. n=4, two-way analysis of variance with Sidak's multiple comparisons test.

750 c. EdU flow cytometry were performed to evaluate the effect of sEVs on the proliferation of
751 NSCLC cells.

752 d. Western blot analysis of the typical sEVs markers CD63, TSG101, and Alix. n=3; Student's
753 two-sided unpaired t test.

754 e. The concentration of the sEVs were detected by NanoSight Analysis. n=3; Student's two-sided
755 unpaired t test.

756 f. CCK-8 assays were performed to evaluate the rescue effect of GW4869 on the proliferation of
757 NSCLC cells co-cultured with MLO-Y4 cells. n=4, two-way analysis of variance with Sidak's
758 multiple comparisons test.

759 g. EdU flow cytometry were performed to evaluate the rescue effect of GW4869 on the
760 proliferation of NSCLC cells co-cultured with MLO-Y4 cells.

761 no significance(ns) $P>0.05$, *$P < 0.05$, **$P < 0.01$, ***$P < 0.001$, ****$P < 0.0001$.

762 **Figure 3**

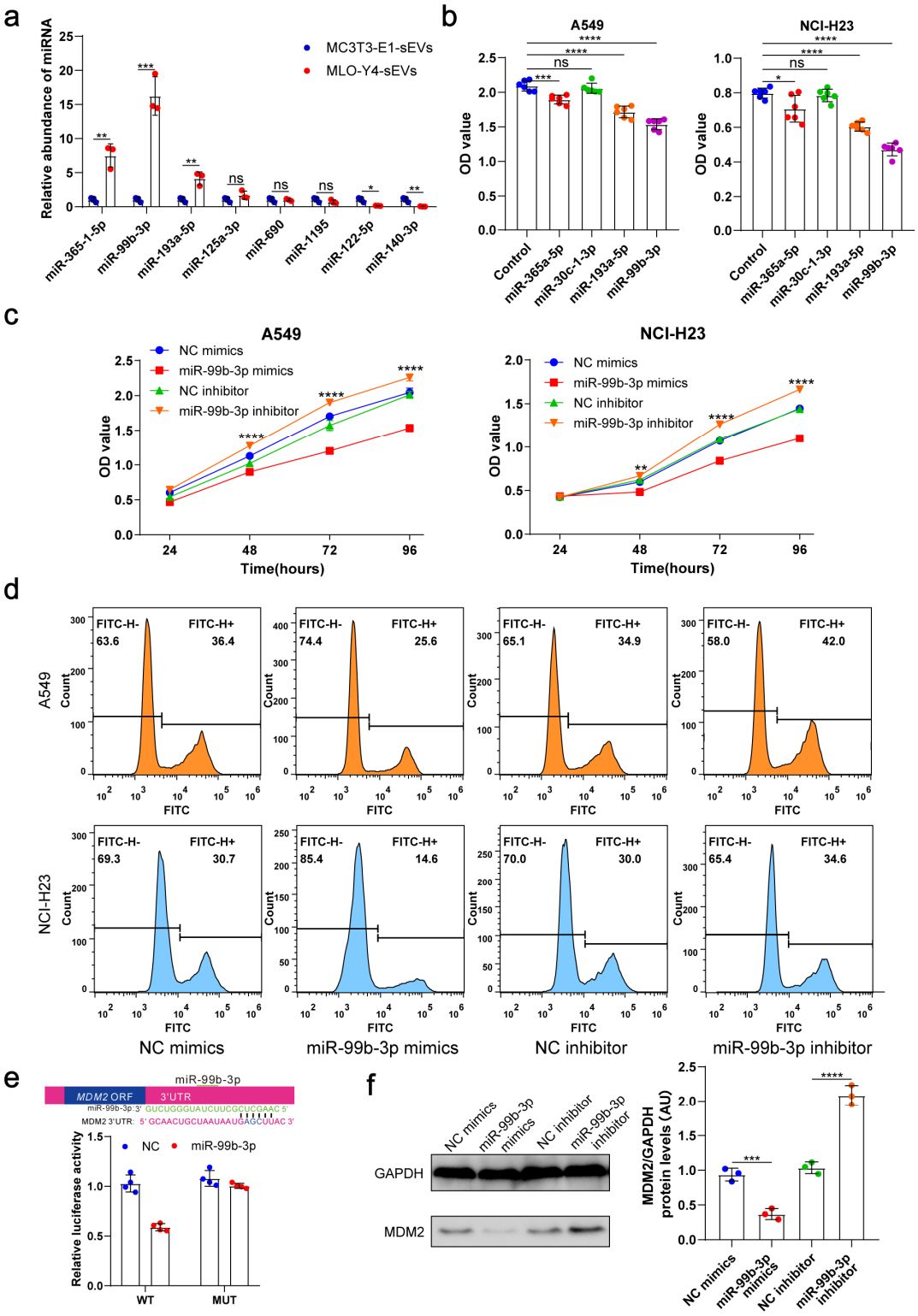
a
Relative abundance of miRNA
MC3T3-E1-sEVs
MLO-Y4-sEVs
miR-365-1-5p
miR-99b-3p
miR-193a-5p
miR-125a-3p
miR-690
miR-1195
miR-122-5p
miR-140-3p
b
A549
NCI-H23
OD value
Control
miR-365a-5p
miR-30c-1-3p
miR-193a-5p
miR-99b-3p
c
A549
NCI-H23
NC mimics
miR-99b-3p mimics
NC inhibitor
miR-99b-3p inhibitor
OD value
Time(hours)
d
A549
NCI-H23
Count
FITC
FITC-H-
FITC-H+
63.6
36.4
74.4
25.6
65.1
34.9
58.0
42.0
69.3
30.7
85.4
14.6
70.0
30.0
65.4
34.6
NC mimics
miR-99b-3p mimics
NC inhibitor
miR-99b-3p inhibitor
e
miR-99b-3p
MDM2 ORF
3'UTR
miR-99b-3p: 3' GUCUGGGUAUCUUCGCUCGAAC 5'
MDM2 3'UTR: 5' GCAACUGCUAAUAAUGAGCUUAC 3'
Relative luciferase activity
NC
miR-99b-3p
WT
MUT
f
NC mimics
miR-99b-3p mimics
NC inhibitor
miR-99b-3p inhibitor
GAPDH
MDM2
MDM2/GAPDH protein levels (AU)

763 **Figure 3. Osteocyte sEVs miR-99b-3p inhibited the proliferation of NSCLC cells by directly**

764 **targeting MDM2.**

765 a. Comparison of relative miR-365-1-5p, miR-99b-3p, miR-193a-5p, miR-125a-3p, miR-690,

766 miR-1195, miR-122-5p, miR-140-3p content between MLO-Y4-sEVs and MC3T3-E1-sEVs by

767 qRT-PCR. n=3, student's two-sided unpaired t test.

768 b. NSCLC cells were transfected with miR-365a-5p, miR-30c-1-3p, miR-193a-5p, miR-99b-3p

769 mimics, or NC (negative control) in DMEM medium. 48 hours later, CCK-8 assays were

770 performed. n=6, one-way analysis of variance with Turkey's multiple comparisons test.

771 c, d. NSCLC cells were transfected with miR-99b-3p mimics, NC mimics, miR-99b-3p inhibitor

772 and NC inhibitor. 48 hours later, EdU flow cytometry were performed. CCK-8 assays were

773 performed at different points in time after transfection. n=6, two-way analysis of variance with

774 Sidak's multiple comparisons test.

775 e. Schematic diagram of putative miR-99b-3p binding sites in the MDM2 3′-UTR. Green letters

776 denote mutation sites. Relative luciferase activities of wild-type (WT) or mutant (MUT) MDM2

777 3′-UTRs were determined in A549 cells, which were co-transfected with the miR-99b-3p mimics

778 or negative control. Luciferase activity was normalized using Renilla. n=4, Student's two-sided

779 unpaired t test.

780 f. MDM2 protein in A549 cells were analyzed by Western blot 72 hours after transfection. n=3;

781 one-way analysis of variance with Turkey's multiple comparisons test.

782 no significance(ns) $P>0.05$, *$P < 0.05$, **$P < 0.01$, ***$P < 0.001$, ****$P < 0.0001$.

783 **Figure 4**

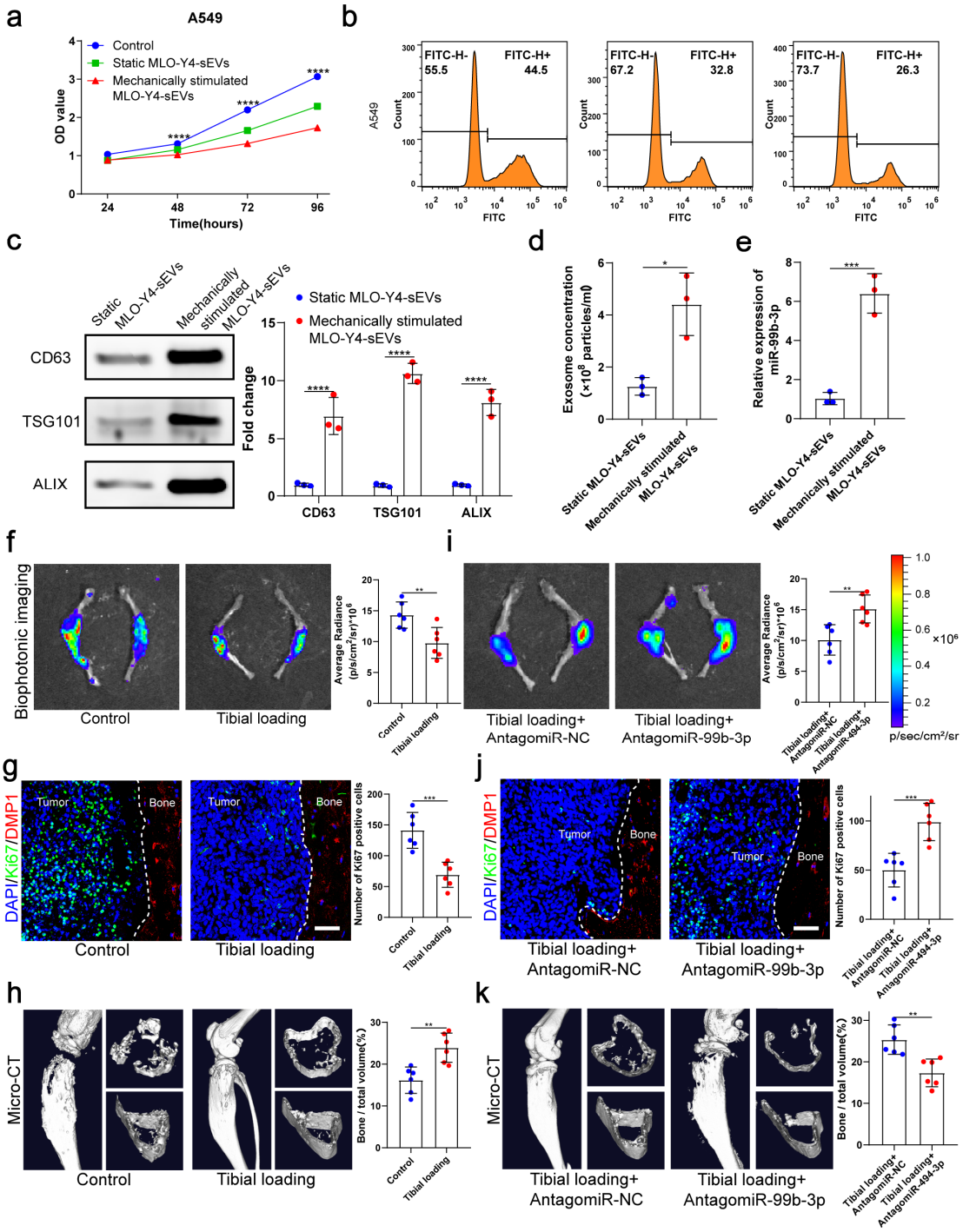
a
A549
Control
Static MLO-Y4-sEVs
Mechanically stimulated MLO-Y4-sEVs
OD value
Time(hours)
b
A549
FITC-H-
FITC-H+
55.5
44.5
67.2
32.8
73.7
26.3
Count
FITC
c
Static MLO-Y4-sEVs
Mechanically stimulated MLO-Y4-sEVs
CD63
TSG101
ALIX
Fold change
d
Exosome concentration (×10^8 particles/ml)
Static MLO-Y4-sEVs
Mechanically stimulated MLO-Y4-sEVs
e
Relative expression of miR-99b-3p
f
Biophotonic imaging
Control
Tibial loading
Average Radiance (p/s/cm²/sr)*10^6
i
Tibial loading+ AntagomiR-NC
Tibial loading+ AntagomiR-99b-3p
Tibial loading+ AntagomiR-494-3p
p/sec/cm²/sr
g
DAPI/Ki67/DMP1
Tumor
Bone
Number of Ki67 positive cells
j
h
Micro-CT
Bone / total volume(%)
k

784 **Figure 4. Mechanical stimulation increased the release of sEVs from osteocytes and**
785 **enhanced inhibitory effect of osteocytes on the proliferation of NSCLC cells.**
786 a. MLO-Y4 cells were mechanically stimulated by stretching at 12% strain at a 1.25 Hz frequency
787 for 12 h, and sEVs were extracted from the conditioned medium. CCK-8 assays were performed
788 to evaluate the effect of sEVs on the proliferation of A549 cells. n=4, two-way analysis of
789 variance with Sidak's multiple comparisons test.
790 b. EdU flow cytometry were performed to evaluate the effect of sEVs on the proliferation of A549
791 cells.
792 c. Western blot analysis of the typical sEVs markers CD63, TSG101, and Alix. n=3, student's
793 two-sided unpaired t test.
794 d. Concentration of sEVs was detected by NanoSight analysis. n=3, student's two-sided unpaired t
795 test.
796 e. Mechanical loading was applied to the tibiae with bone metastasis via direct implantation of
797 GFP-LLC into tibia of mouse. qRT-PCR identification of miR-99b-3p in sEVs. n=3, student's
798 two-sided unpaired t test.
799 An intraosseous model of bone metastasis was used via direct implantation of murine Lewis lung
800 carcinoma (LLC) cells expressing green fluorescent protein (GFP) into tibia of mouse. Mice were
801 subsequently randomized into tumor-bearing only (control), tibial loading, tibial
802 loading+antagomiR-NC and tibial loading+antagomiR-99b-3p groups. Four weeks later, mice
803 were sacrificed.
804 f, i. Representative biophotonic images and quantification of fluorescence signal in hindlimb
805 bones of mice. n=6, one-way analysis of variance with Turkey's multiple comparisons test.

806 g, j. Representative immunofluorescence staining images of Ki-67(green), DMP1(red), and DAPI

807 (blue) in the tibia of mice with bone metastases and quantification of the number of Ki-67-positive

808 cells in the images. The dashed line indicates the boundary between bone and tumor. Scale bars:

809 50 μm. n=6, one-way analysis of variance with Turkey's multiple comparisons test.

810 h, k. Representative micro-CT imaging and quantitation of the tibia (bone/total volume) in mice.

811 n=6, one-way analysis of variance with Turkey's multiple comparisons test.

812 no significance(ns) $P>0.05$, *$P < 0.05$, **$P < 0.01$, ***$P < 0.001$, ****$P < 0.0001$.

Figure 5

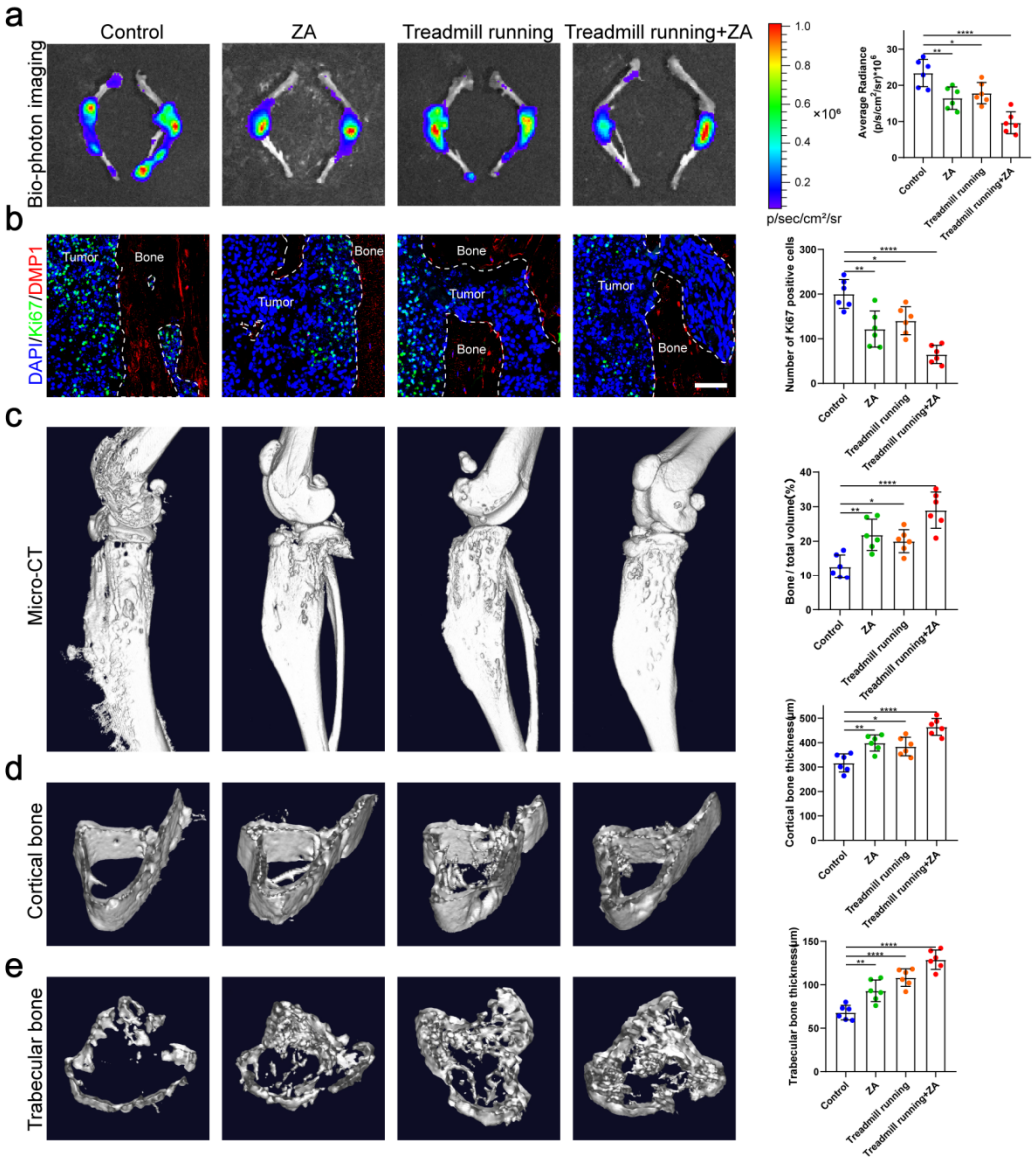
a
Control
ZA
Treadmill running
Treadmill running+ZA
Bio-photon imaging
p/sec/cm²/sr
Average Radiance (p/s/cm²/sr)*10⁶
b
DAPI/Ki67/DMP1
Tumor
Bone
Number of Ki67 positive cells
c
Micro-CT
Bone / total volume(%)
d
Cortical bone
Cortical bone thickness(μm)
e
Trabecular bone
Trabecular bone thickness(μm)

814 **Figure 5. Moderate exercise combined with zoledronic acid effectively suppressed the**

815 **progression of bone metastasis of NSCLC.**

816 An intraosseous model of bone metastasis was used via direct implantation of murine Lewis lung

817 carcinoma (LLC) cells expressing green fluorescent protein (GFP) into tibia of mouse. Mice were

818 subsequently randomized into tumor-bearing only (control), zoledronic acid (ZA), treadmill

819 running, and treadmill running combined zoledronic acid (treadmill running+ZA) groups. Four

820 weeks later, mice were sacrificed.

821 a. Representative biophotonic images and quantification of fluorescence signal in hindlimb bones

822 of mice. n=6, one-way analysis of variance with Turkey's multiple comparisons test.

823 b. Representative immunofluorescence staining images of Ki-67(green), DMP1(red), and DAPI

824 (blue) in the tibia of mice with bone metastases and quantification of the number of Ki-67-positive

825 cells in the images. The dashed line indicates the boundary between bone and tumor. Scale bars:

826 50 μm. n=6, one-way analysis of variance with Turkey's multiple comparisons test.

827 c-e Representative micro-CT imaging and quantitation of the tibia (bone/total volume, cortical

828 bone thickness, trabecular bone thickness) in mice. n=6, one-way analysis of variance with

829 Turkey's multiple comparisons test.

830 no significance (ns) $P>0.05$, *$P < 0.05$, **$P < 0.01$, ***$P < 0.001$, ****$P < 0.0001$.

831 **Figure 6**

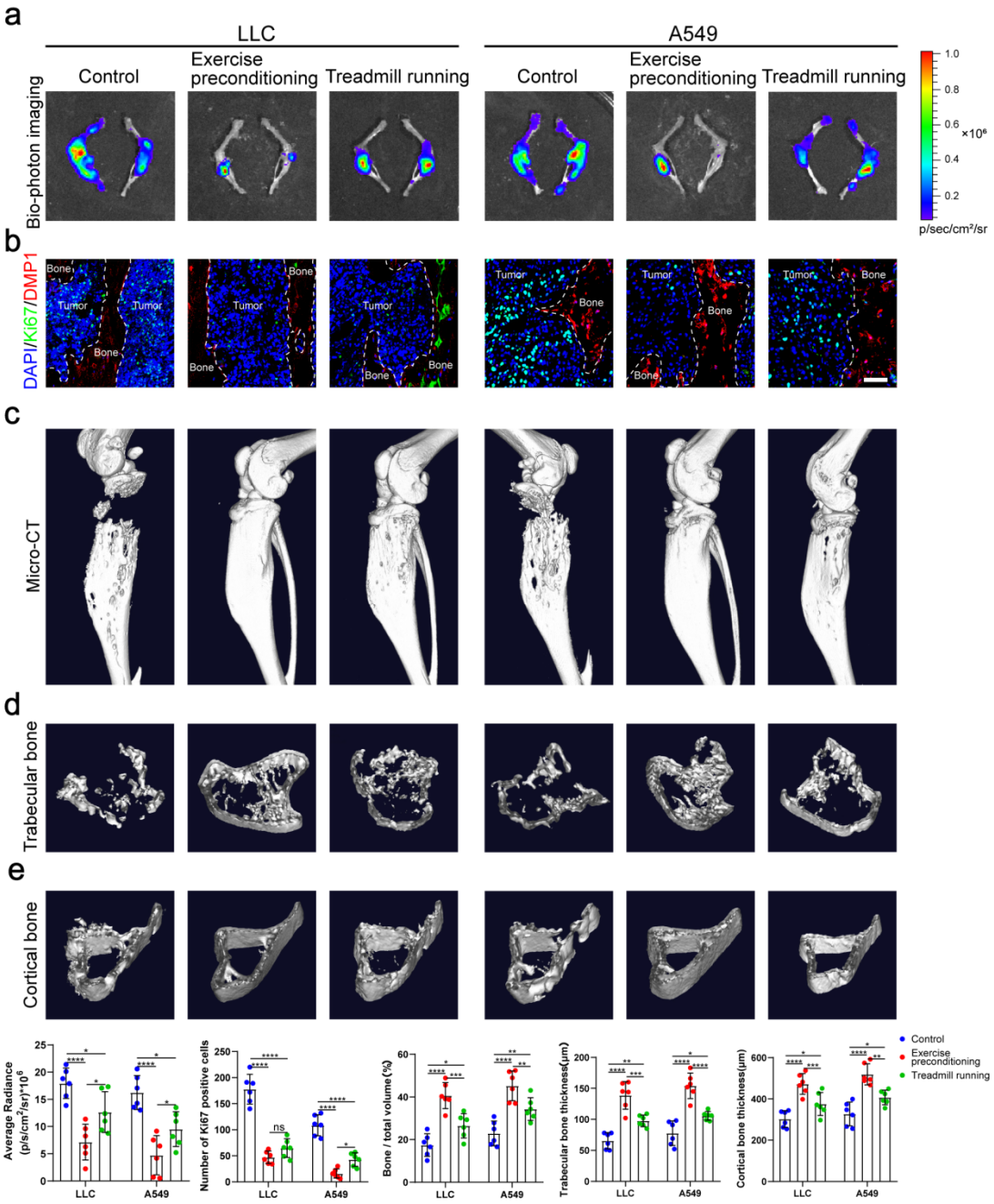
a
LLC
A549
Control
Exercise preconditioning
Treadmill running
Control
Exercise preconditioning
Treadmill running
Bio-photon imaging
1.0
0.8
0.6
×10⁶
0.4
0.2
p/sec/cm²/sr
b
DAPI/Ki67/DMP1
Bone
Tumor
c
Micro-CT
d
Trabecular bone
e
Cortical bone
Average Radiance (p/s/cm²/sr)*10⁶
Number of Ki67 positive cells
Bone / total volume (%)
Trabecular bone thickness(μm)
Cortical bone thickness(μm)
LLC
A549
Control
Exercise preconditioning
Treadmill running

832 **Figure 6. Exercise preconditioning effectively suppressed the progression of bone metastasis**

833 **of NSCLC.**

834 An intraosseous model of bone metastasis was used via direct implantation of NSCLC cells (LLC

835 and A549) into tibia of mouse. Mice were subsequently randomized into tumor-bearing only

836 (control), treadmill running before and after implantation of NSCLC cells into tibia (exercise

837 preconditioning), and treadmill running after implantation of NSCLC cells into tibia (treadmill

838 running) groups. For exercise preconditioning group, mice were subjected to 4 weeks of treadmill

839 exercise before implantation of NSCLC cells into tibia of mouse. Four weeks after implantation,

840 mice were sacrificed.

841 a. Representative biophotonic images and quantification of fluorescence signal in hindlimb bones

842 of mice. n=6, one-way analysis of variance with Turkey's multiple comparisons test.

843 b. Representative immunofluorescence staining images of Ki-67(green), DMP1(red), and DAPI

844 (blue) in the tibia of mice with bone metastases and quantification of the number of Ki-67-positive

845 cells in the images. The dashed line indicates the boundary between bone and tumor. Scale bars:

846 50 μm. n=6, one-way analysis of variance with Turkey's multiple comparisons test.

847 c-e Representative micro-CT imaging and quantitation of the tibia (bone/total volume, cortical

848 bone thickness, trabecular bone thickness) in mice. n=6, one-way analysis of variance with

849 Turkey's multiple comparisons test.

850 no significance (ns) $P>0.05$, *$P < 0.05$, **$P < 0.01$, ***$P < 0.001$, ****$P < 0.0001$.

851 **Figure 7**

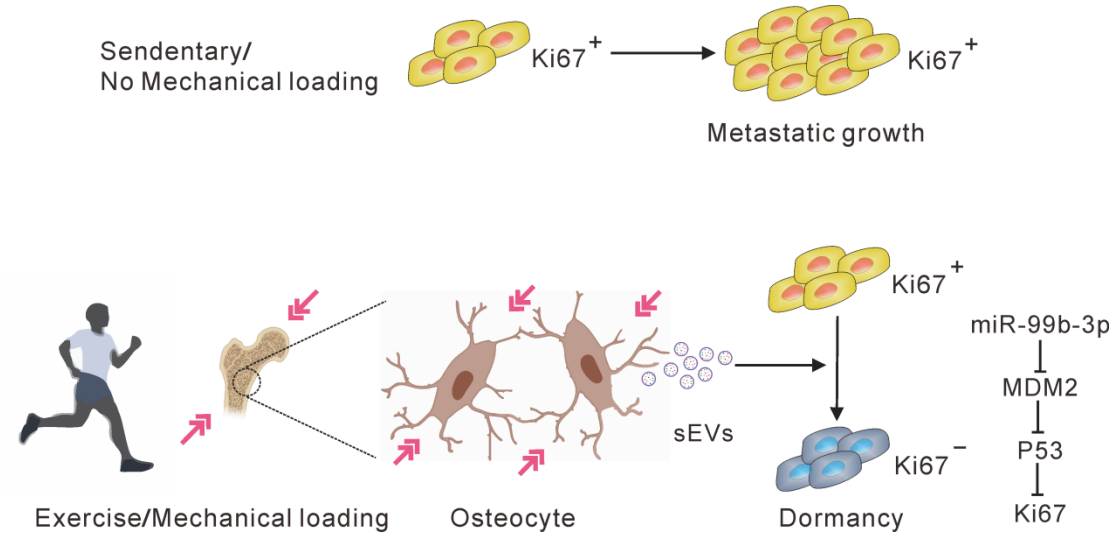

852 **Figure 7. A hypothetic model depicting osteocytes induce and maintain tumor dormancy in**

853 **bone metastasis of non-small cell lung cancer.**

854 Osteocytes, sensing mechanical stimulation generated by exercise or mechanical loading, inhibit

855 the proliferation and sustain the dormancy of NSCLC cells by releasing sEVs with tumor

856 suppressor miRNAs, such as miR-99b-3p, which inhibits the proliferation of NSCLC cells by

857 directly targeting MDM2.